energies

MDPI

Article

Stepwise Multi-Objective Parameter Optimization Design of LLC Resonant DC-DC Converter

Miaomiao Yin * and Quanming Luo

State Key Laboratory of Power Transmission Equipment Technology, School of Electrical Engineering, Chongqing University, Chongqing 400044, China; lqm394@126.com
* Correspondence: 202111021069t@cqu.edu.cn

Abstract: The LLC resonant converter, which is extensively utilized across various industrial fields, significantly depends on its parameters for performance optimization. This paper establishes a time-domain analytical model for the LLC resonant converter under Pulse Frequency Modulation (PFM) and proposes a multi-objective parameter optimization design method with stepwise constraints. The proposed method limits the resonant capacitor voltage while ensuring that the converter meets the voltage gain requirement and realizes Zero-Voltage Switching (ZVS). The converter's performance is then optimized with the objective of minimizing the switching frequency range, the resonant inductor current, and the RMS value of the switching current on the secondary side. Compared with the existing methods, the proposed method has the advantages of comprehensive consideration and wide application scenarios. Finally, a 1200 W experimental prototype was fabricated, with experimental results verifying the feasibility of the proposed optimization design method and demonstrating that the prototype's maximum efficiency reaches 96.54%.

Keywords: DC/DC; intelligent optimization algorithm; LLC resonant converter; parameter design

Citation: Yin, M.; Luo, Q. Stepwise Multi-Objective Parameter Optimization Design of LLC Resonant DC-DC Converter. *Energies* **2024**, *17*, 1919. https://doi.org/10.3390/en17081919

Received: 20 March 2024
Revised: 11 April 2024
Accepted: 15 April 2024
Published: 17 April 2024

1. Introduction

Owing to its high efficiency, robust voltage regulation, and the facile implementation of Zero-Voltage Switching (ZVS) and Zero-Current Switching (ZCS), the LLC resonant converter is extensively utilized in applications such as vehicle chargers, communication power supplies, LED drivers, and power adapters [1]. It ranks among the most prevalently employed isolated converters.

Pulse Frequency Modulation (PFM) is the predominant modulation method for LLC resonant converters. While PFM exhibits limitations such as suboptimal voltage regulation and elevated switching frequencies under light load conditions [2], it offers benefits such as straightforward implementation, superior transient characteristics, and soft switching across a broad spectrum of medium to heavy load conditions. Consequently, investigating the analysis and design methodologies for LLC resonant converters under PFM modulation becomes imperative.

LLC resonant converters are analyzed primarily through two methods: frequency domain analysis (FDA) and time domain analysis (TDA). The frequency domain analysis method is further divided into the first harmonic approximation (FHA) and the extended harmonics approximation (EHA), where the FHA only considers the role of the fundamental waveform component [3,4]. Conversely, EHA enhances analytical precision by incorporating the effects of additional subharmonic components [5]. However, the analytical complexity of EHA escalates with an increase in the number of incorporated harmonic components. When the converter operates in the current intermittent mode, EHA does not significantly improve the accuracy of the analysis. The time-domain analysis method offers an accurate assessment of a converter's operational characteristics by solving its state equations across different modes. Despite the complexity of time-domain analysis,

its depth and precision are advantageous for thoroughly understanding and enhancing converter efficiency and reliability.

Numerous studies have focused on parametric design analysis through time-domain models. Refs. [6–8] thoroughly describe establishing a time-domain model for LLC converters, advocating for optimizing system maximum voltage gain at the peak gain point. This approach ensures a monotonic voltage gain curve for the converter. However, it introduces the possibility of the converter operating in PN or PON modes, which may prevent the primary-side switches from achieving ZVS, thereby increasing switching losses and reducing the converter's transmission efficiency. Ref. [9] expanded the scope by integrating a loss model into the design process, advocating for a computer-aided optimization framework. However, this method's reliance on detailed component introduces complexity and potential inaccuracies.

Transitioning towards application-specific optimization, Ref. [10] adapted the LLC resonant converter design to accommodate the nonlinear charging profiles of lithium-ion batteries, marking a departure from conventional assumptions of resistive loads. Concurrently, Ref. [11] introduced the Time-Weighted Average Efficiency (TWAE) index, enhancing efficiency metrics for battery charging, albeit with limited applicability beyond electric vehicle charging solutions. Ref. [12] proposed a comprehensive parameter optimization strategy, liberating the design from previously constrained operational modes. However, this approach grapples with search efficiency and achieving optimal solutions. Ref. [13] contributed a generalized analysis suitable for varied loads by modeling LED loads as segmented linear circuits, demonstrating the adaptability of time-domain analysis across different applications.

Recent studies, including those by [1,14], have focused on optimizing LLC resonant converters within specific operational modes, employing loss models and multi-objective optimization strategies to enhance precision and efficiency. Ref. [15] further extended the optimization framework to consider the RMS current of the resonant inductor, integrating a comprehensive set of design considerations facilitated by the Particle Swarm Optimization (PSO) algorithm. In addition, there are studies focusing on further optimization of the circuit parameters of LLC-DC Transformers considering the current intermittent mode [16].

Combined with the analysis of the above literature, a comparative table of methods for parameter design optimization of LLC converter is given here, as shown in Table 1. Most parametric design approaches focus only on the voltage gain range and primary side-switching ZVS implementation, which has inherent limitations. Limiting the converter's mode of operation to a fixed mode affects the converter's performance.

Additionally, it is difficult to model losses very accurately, and this approach can only be used to parameterize the circuit after the circuit device selection has been determined, rather than after the circuit parameterization has been performed and a more appropriate device has been selected based on the performance of the converter. Limited research has addressed optimizing the LLC converter's switching frequency range. Optimization reliant on a fixed switching frequency range does not ensure its optimality. This may result in the range being too wide, which can negatively impact the converter's operating performance, or too narrow, leading to the loss of a more optimal solution.

Considering the above factors, a multi-objective parameter optimization method with stepwise constraints is proposed in this paper. First, the preliminary design space for parameters is constrained by voltage gain requirements within the predefined switching frequency range. The parameters in the preliminary parameter design space ensure that the converter operates within the set operating region and realizes the basic design requirements. Then, the current RMS of the vice-side switches, the resonant inductor current RMS and the switching frequency range are taken as the optimization objectives, and the resonant capacitor voltage stress is also taken into account, and an intelligent optimization algorithm, the Adaptive Non-dominated Sorting Genetic Algorithm (ANSGA-III) [17,18], is used to carry out a preliminary constrained design space for the multi-objective optimization to improve the performance of the converter.

Table 1. Comparisons among different design methods.

Methods	Analysis Model	Voltage Gain	Consideration	Optimization Objective	Operating Mode
[6–8,12]	TDM	Wide range	Voltage gain	-	Peak voltage gain
[9]	TDM	Unity	-	Loss models	-
[10]	FHA+TDM	Wide range	ZVS, voltage gain	-	Depending on the battery characteristics
[11]	TDM	Wide range	ZVS, voltage gain	TWAE	Depending on the battery characteristics
[13]	TDM	Wide range	ZVS, voltage gain	Loss models	-
[1]	TDM	Wide range	ZVS, voltage gain, $u_{Cr\max}$, $f_{s\min}$	Loss models	PO mode
[15]	TDM	Wide range	ZVS, voltage gain, $u_{Cr\max}$, $f_{s\min}$	$i_{Lr\mathrm{RMS}}$	-
[14]	data-driven surrogate model	Wide range	ZVS, voltage gain, $u_{Cr\max}$	$i_{Lr\mathrm{RMS}}$, $i_{2\mathrm{RMS}}$, P_{Fe}	PO mode
[16]	TDM	Nearby unity	ZVS, parasitic capacitance	Loss models	-
Proposed	TDM	Wide range	ZVS, voltage gain, $u_{Cr\max}$	$i_{Lr\mathrm{RMS}}$, $i_{Q1\mathrm{RMS}}$, Switching frequency range	Voltage gain monotonic region

$u_{Cr\max}$ is the maximum value of the peak capacitance voltage, $i_{Lr\mathrm{RMS}}$ is the RMS value of the resonant inductor current, $i_{2\mathrm{RMS}}$ is the rms value of the rectifier current on the secondary side, $i_{Q1\mathrm{RMS}}$ is the rms value of the current of the secondary side switching, and P_{Fe} is the transformer core loss.

2. The Analysis of the LLC Converter

The circuit topology of the full-bridge LLC resonant converter is shown in Figure 1, in which U_1 and U_2 represent the input and output voltages, respectively, with L_m denoting the excitation inductance and n (N_p:N_s) indicating the turns ratio of transformer T, while L_r, C_r, and L_m constitute the resonant network. The time domain analysis model is analyzed and supplemented for the LLC converter as follows. The time-domain modeling assumes idealized switches, disregarding parasitic capacitance and losses. This simplification aims to streamline the analysis, with fewer complexities than practical implementations.

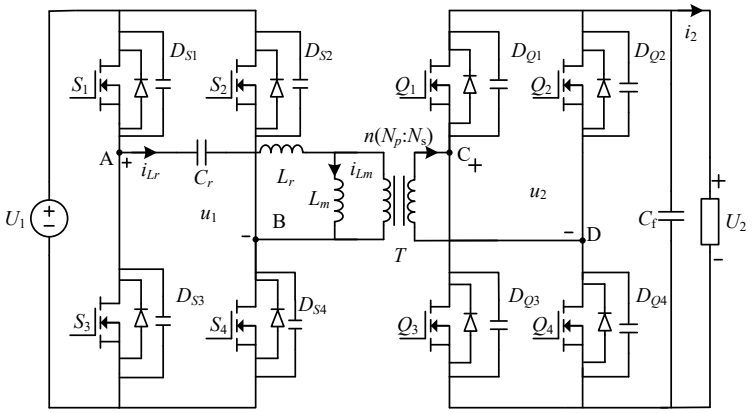

Figure 1. Full bridge LLC resonant converter.

2.1. Operating Mode Analysis

For the convenience of the analysis, it is necessary to normalize the variables, as shown in Table 2, where the benchmark values are shown:

$$f_{base} = f_r = \frac{1}{2\pi\sqrt{L_r C_r}}, Z_{base} = Z_r = \sqrt{\frac{L_r}{C_r}}, U_{base} = U_1 \tag{1}$$

In the first half-cycle (S_1, S_4 conduction phase), the LLC converter's operating stages are categorized into three types based on the rectifier bridge's conduction: The P stage corresponds to the conduction of anti-parallel diodes D_{Q1} and D_{Q4}, the N stage to D_{Q2} and D_{Q3}, and the O stage occurs when diodes D_{Q1} through D_{Q4} are all off. The equivalent circuits for different operating stages are shown in Figure 2. By writing and solving the state equations for the P, O, and N stages, one can derive the corresponding time-domain expressions with unknowns, as detailed in Appendix A.

Table 2. Variables and normalization.

Circuit Variable	Symbol	Normalized Variable
Resonant frequency	$f_r = 1/2\pi\sqrt{L_r C_r}$	-
Characteristic impedance	$Z_r = \sqrt{L_r/C_r}$	-
Excitation inductance ratio	k_m=L_m/L_r	-
Voltage gain	$M = nU_2/U_1$	-
Switching frequency	f_s	$f_n = f_s/f_r$
Time	t	$\theta = \omega_r t = 2\pi f_r t$
Reflected output current	I_2/n	$I_n = Z_r I_2/U_1/n$
Reflected output voltage	nU_2	$M = nU_2/U_1$
Transmission power	P_o	$P_n = I_n M$

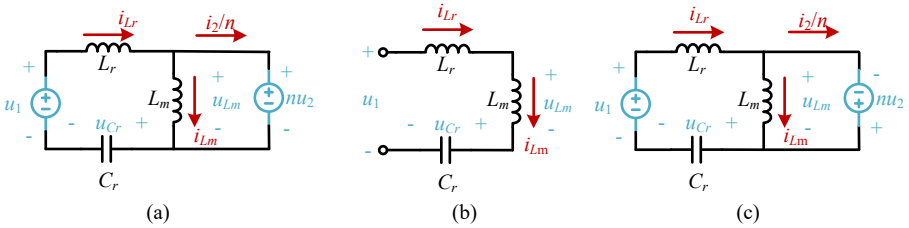

Figure 2. Equivalent circuit of the LLC resonant tank in different operating stages. (**a**) P stage. (**b**) O stage. (**c**) N stage.

The rectifier bridge arm is off in O stage, so the converter participates in energy transfer only in P and N stages and the normalized output current is shown:

$$I_n = \frac{f_n}{\pi}\left[\int_0^{\theta_P}\left(i_{L_{rPn}} - i_{L_{mPn}}\right)d\theta + \int_0^{\theta_N}\left(i_{L_{mNn}} - i_{L_{rNn}}\right)d\theta\right] \tag{2}$$

Detailed methodologies for the exact solution procedure are extensively delineated in the existing literature [6–8] and will thus not be reiterated here. The following succinctly outlines the principles underlying the solution of the time-domain equations. The converter operates in various modes by combining the three stages in different sequences. Each mode of operation is limited by the boundary conditions of neighboring stage nodes and switching moments. This includes maintaining the continuity of capacitive voltages and inductive currents between stages. Additionally, the terminal values of i_{L_r}, i_{L_m}, and u_{C_r} should oppose their initial values at steady state, ensuring symmetry. Finally, it is also necessary to satisfy Equation (2) to ensure power conservation. Adhering to these constraints, one can derive the circuit equations for each of the six modes by numerically solving them, using known values for the load and switching frequency. The resultant circuit waveforms for these modes are detailed in Appendix B.

Beyond the critical mode and the six primary modes of operation, PFM modulation introduces two special modes in which no power is transferred to the output. The first, known as the O mode, involves an open load. The second mode is characterized by an output short-circuit condition. A key distinction between these modes is operational: in the O mode, the output current (I_n) equals zero, indicating no load condition. Conversely, in the output short-circuit mode, the voltage gain (M) is zero, denoting that no voltage is applied across the output despite the presence of a short circuit.

In the O mode, all the energy is circulated in the resonant tank, and the rectifier diode on the secondary side is turned off, $|u_{L_{mn}}| \leq M$. From this, it can be deduced that the voltage gain M_{O} in the O mode needs to satisfy the condition as shown:

$$M_{\mathrm{O}} \geq \frac{k_m}{k_m+1} \frac{1}{\cos\left(\pi/\left(2f_n\sqrt{k_m+1}\right)\right)} \tag{3}$$

The output short-circuit condition exclusively occurs in PN and NP modes, where the durations of P and N stages are identical. Under these conditions, the solution for the normalized output current $I_{n\mathrm{short}}$ in the short circuit mode is as follows:

$$I_{n\mathrm{short}} = \begin{cases} 2f_n(1-\sec(\pi/2f_n))/\pi, f_n < 1 \\ 2f_n(\sec(\pi/2f_n)-1)/\pi, f_n > 1 \end{cases} \tag{4}$$

Despite its rare inclusion in previous time-domain analytical models, considering the short-circuit case is essential for comprehensive time-domain modeling. This is because inaccuracies arise in the time-domain model when I_n exceeds Inshort for a given f_n. Moreover, short-circuited currents reveal a limitation in the converter's maximum power transmission capacity, particularly when $f_n \neq 1$.

2.2. Operating Mode Judgment

Solving the time-domain equations for circuits in various operating modes is critical. Subsequently, analyzing the conditions under which modes switch is imperative. This systematic analysis facilitates the determination of the converter's operating mode across different loads, switching frequencies, and voltage gains, thereby establishing a critical benchmark for mode classification and optimization.

Figure 3 illustrates the typical mode boundaries and distributions for the LLC resonant converter on the f_n-I_n and f_n-M planes, offering visual guidance on mode transitions. The PO, PON, and PN modes operate in the below-resonance region (BRR) ($f_n < 1$). The NP and NOP modes operate in the above-resonance region (ARR) ($f_n > 1$). Uniquely, the OPO mode can operate in all the above regions.

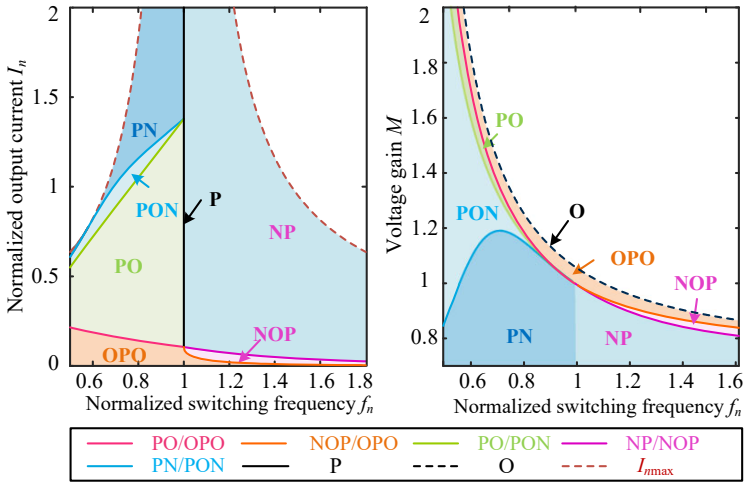

Figure 3. Modes distribution of LLC in f_n-I_n plane and f_n-M plane.

This demonstrates that, with a known f_n, determining the operating mode of the converter is straightforward, and can be achieved by analyzing both the normalized output current I_n and the voltage gain M.

The voltage gain surface in the f_n-I_n plane can be obtained via a numerical calculation, as shown in Figure 4. Based on Figure 4, the gain curves for various I_n values can be obtained, as depicted in Figure 5. Clearly, within the BRR, the gain curves for varying loads display a distinct peak gain (M_{peak}). Each one is uniquely associated with a specific f_n. The yellow dashed lines in Figure 5 represent the curves comprising the voltage peak gain points.

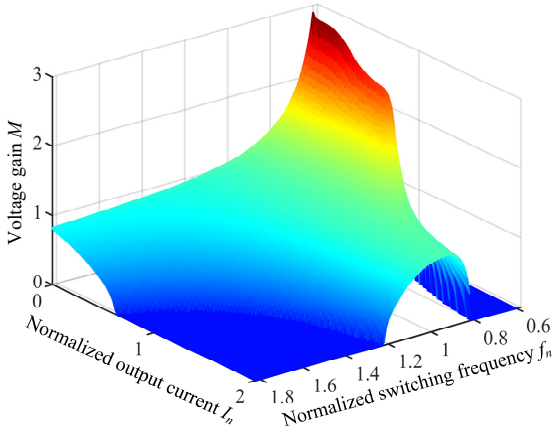

Figure 4. Variation in I_n with M and f_n.

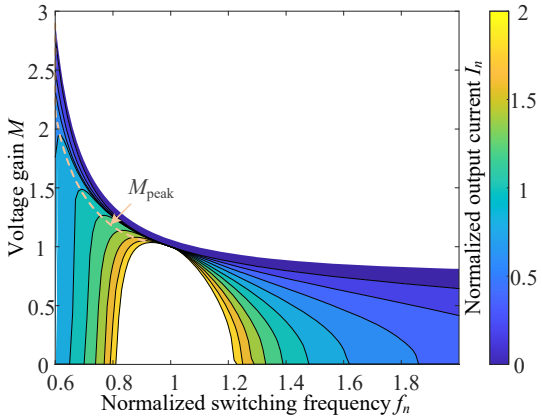

Figure 5. Contour projection of I_n in the f_n-M plane.

For optimal control simplicity, it is essential that the converter's gain curve remains monotonic. In this context, the operating point at the peak voltage gain becomes a critical factor. The peak voltage gain point occurs in PON mode and PN mode when the resonant current i_{L_r} is zero when the switches are turned off on the primary side [6]. Based on this condition, the equation for the peak gain can be solved with any of the variables identified in f_n, M_{peak}, and I_n.

Given the non-monotonic nature of the voltage gain curve within the BRR, determining the mode solely based on M and I_n presents greater complexity compared to when f_n has been identified. As shown in Figure 6, the contour of I_n in the f_n-M plane can be obtained from Figure 4. In the BRR, the contour of f_n has a cross-section in the I_n-M plane, i.e., the same set of M and I_n will be solved for two f_n solutions, possibly corresponding to two different modes.

However, accurate mode determination based on voltage gains M and I_n, as well as the successful solution of corresponding time-domain equations, necessitates operation within

a region defined by a monotonic voltage gain curve. Therefore, when optimizing parameter design, it is important to first impose constraints to ensure that the converter operates within this region. Adhering to this operational prerequisite allows subsequent optimization efforts, particularly regarding the switching frequency range, to be more effective.

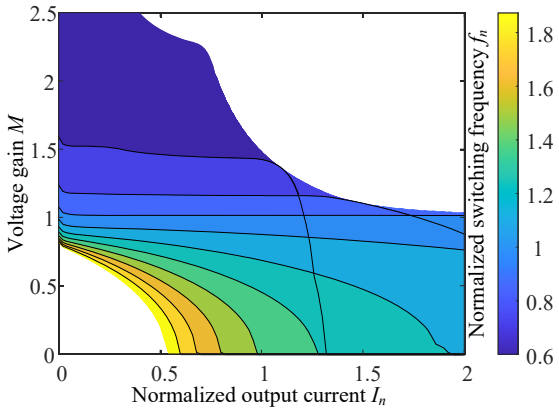

Figure 6. Contour projection of f_n in the I_n-M plane.

3. A Step-By-Step Multi-Objective Approach to Parameter Design

Categorizing the parameters and state variables of the LLC converter into three distinct groups—system requirements and parameters, circuit parameters, and component state variables—facilitates a more structured analysis and design optimization, as depicted in Figure 7. The system requirements encompass the essential design specifications that dictate the converter's functionality, whereas the component state variables provide insights into the converter's performance and, to some extent, reflect the converter's performance. Optimizing the design of circuit parameters is crucial for unlocking the full efficient conversion potential of the LLC resonant converter, all while adhering to fundamental design requirements.

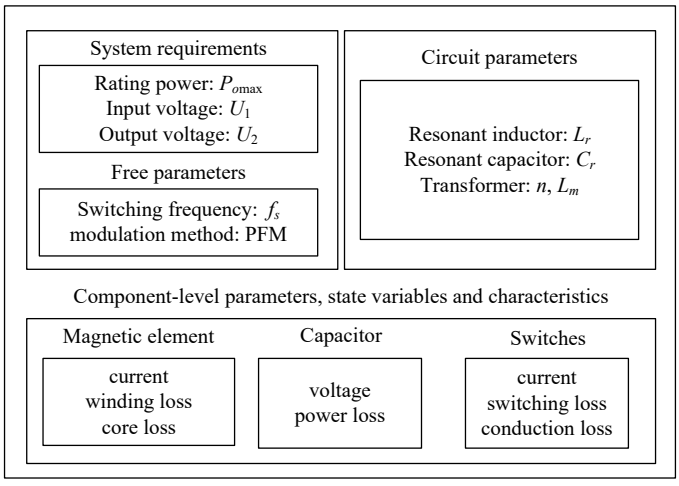

Figure 7. Relationships among system requirements, circuit parameters, and state variables.

3.1. Parameter Design Requirements

As detailed in Table 3, the input voltage is set at 400 V, with the output voltage varying between 42 and 57 V. Given the constraints posed by EMI, power density requirements, and switching device performance, the acceptable switching frequency range has been selected as 60–200 kHz, which is equivalent to a normalized frequency range of 0.6–2. It is important to note that the given maximum range of switching frequencies is not the actual operating range.

Table 3. Parameter design requirements.

System Requirements	Range
Input voltage U_1	400 V (DC)
Output voltage U_2	42–57 V (DC)
Switching frequency f_s	60–200 kHz
Rated power $P_{o\max}$	1200 W

3.2. Main Circuit Parameter Design Optimization

In the design of the LLC resonant converter's main circuit, parameters L_r, C_r, and L_m are normalized to f_r, Z_r, and k_m for a unified analysis, as detailed in Table 2. With the switching resonant frequency identified as f_r, establishing values for n, Z_r, and k_m directly determines the main circuit parameters for the LLC resonant converter. Hence, the goal of parameter optimization is identifying the point or region within the k_m-Z_r plane—constrained by specific n values—that meets the design requirements.

Figure 8 illustrates the process of constraining the preliminary parameter design space using voltage gain limits. This constraint guarantees that the chosen parameters enable operation within the monotonic section of the voltage gain curve and satisfy the voltage gain range. Subsequent optimization within this preliminary design space focuses on refining the converter's performance by adjusting device parameters, state variables, and feature characteristics to meet specific design objectives.

3.2.1. Preliminary Parameterization of Design Space Constraints

In the P mode, the voltage gain remains constant regardless of the load, and the resonant inductor current has a sinusoidal shape with minimal losses. Therefore, the transformer turns ratio, n, can be limited initially based on the voltage gain range to ensure that the converter operates in the P mode ($M = 1$).

$$M_{\min} = \frac{nU_{2\min}}{U_1} \le 1 \le M_{\max} = \frac{nU_{2\max}}{U_1} \tag{5}$$

The range of converter turns n can be obtained as

$$\frac{U_1}{U_{2\max}} \le n \le \frac{U_1}{U_{2\min}} \tag{6}$$

According to the design parameters in Table 3, the range of n can be obtained as $7.02 \le n \le 9.524$. To ensure that the theoretical design parameters can be practically applied to the transformer, the turns ratio n is the ratio of integer to integer. For the power-level determination, according to the AP method approximation, the core type of the transformer can be chosen. Here, a certain margin is taken, and the core model of the transformer is selected as PQ5050, while N_s is taken to be a maximum of 3 turns. With N_s as the denominator and N_p as the numerator, all possible values of the number of transformer turns n are [22/3, 15/2, 23/3, 8, 25/3, 17/2, 26/3, 9, 28/3, 19/2].

The optimized circuit parameters need to ensure that the gain characteristics cover the entire operating region completely and the gain curve needs to be monotonic. The need for voltage gain can be analyzed in both the BRR and ARR. In the BRR, the operating region of the converter is limited by the minimum switching frequency $f_{n\min}$ and the peak gain M_{peak} in order to ensure the monotonicity of the voltage gain curve and the maximum voltage gain requirement.

The ZVS realization of the primary switches must be able to realize the charging and discharging of the switching parasitic capacitance during the dead time to ensure that the voltage is 0 when the switches are turned on. The conditions required to realize the ZVS are shown:

$$Q_{dead} = \int_{t_{off}}^{t_{off}+t_d} i_{Lr}(t)dt \geq 2C_{oss}U_1 \quad (7)$$

where t_{off} is the turn-off moment, i.e., $1/2f_s$, C_{oss} is the value of the output capacitance of the switches on the primary side and t_d is the dead time.

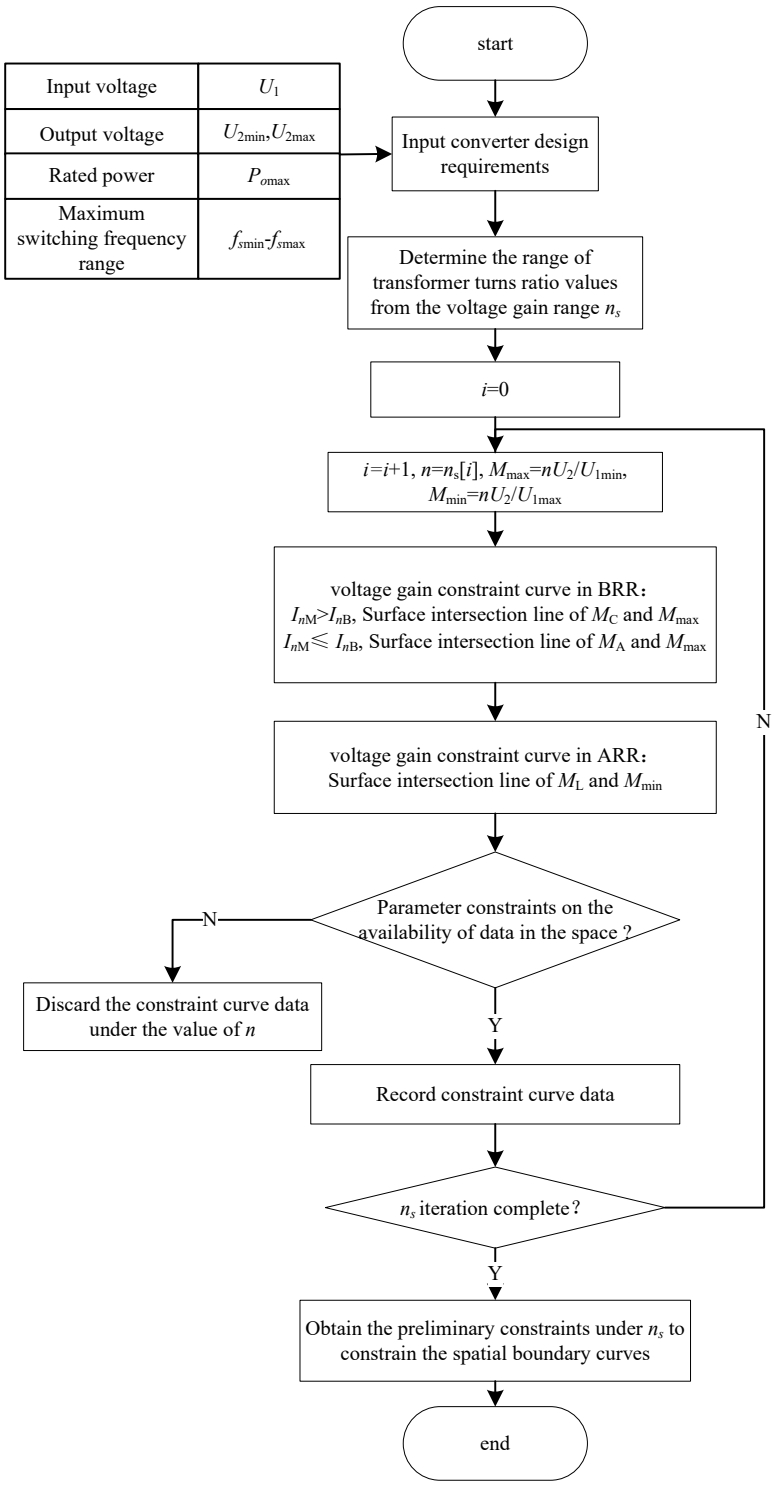

Figure 8. Preliminary parameter design flowchart.

The realization of ZVS includes both the direction and magnitude of the resonant current. The direction of the current needs to be in the reverse diode conduction direction when the switches are turned on. The limiting constraint of peak gain M_{peak} also ensures that the converter satisfies the necessary conditions for ZVS in terms of the current direction.

To ensure that the entire operating range of the converter is within the limited operating region, it is necessary to find the most extreme operating point, i.e., the one that is the most difficult to fulfill. Through Figure 5, it is easy to find that it is most difficult to achieve the desired voltage gain when the output power P_o is at its maximum and the output voltage U_2 is also at its maximum. The normalized output current for this operating condition can be denoted as $I_{n\text{M}}$, as shown:

$$I_{n\text{M}} = \frac{P_{o\,\max}}{nU_{2\,\max}} \frac{Z_r}{U_1} \tag{8}$$

As shown in Table 4, the critical working conditions in the BRR can be categorized into four working conditions: A, B, C, and MM, where A is the working condition at the minimum switching frequency with normalized output current $I_n = I_{n\text{M}}$, B is the working condition in which the minimum switching frequency happens to be the peak gain, C is the working condition in which the peak voltage gain occurs at $I_{n\text{M}}$, and MM is the working condition with voltage gain $M = M_{\max}$ and normalized output current $I_n = I_{n\text{M}}$. MM is the working point with the largest voltage gain and the smallest actual switching frequency. If the MM operating point is within the constrained region, it can fulfill the voltage gain requirement in the BRR.

Table 4. Key operating situations for forward mode in the BRR.

Operating Situations	Known Condition	Results of the Time-Domain Model Solution
A	$f_{n\min}$, $I_{n\text{M}}$	M_{A}
B	$f_{n\min}$	M_{B}, $I_{n\text{B}}$
C	$I_{n\text{M}}$	$f_{n\text{C}}$, M_{C}
MM	$I_{n\text{M}}$, $M_{\max}$	$f_{n\text{MM}}$

To ensure that the converter operates within a given switching frequency range and achieves the required voltage gain in the BRR, it can be discussed in two cases based on the magnitude relationship between $I_{n\text{M}}$ and $I_{n\text{B}}$.

As shown in Figure 9, when $I_{n\text{M}} \le I_{n\text{B}}$, the working condition at point A needs to be analyzed, and if $M_{\text{A}} \ge M_{\max}$ is satisfied, then $f_{n\text{MM}} \ge f_{n\min}$, meaning that the switching frequency is within the required range and the voltage gain requirement is satisfied.

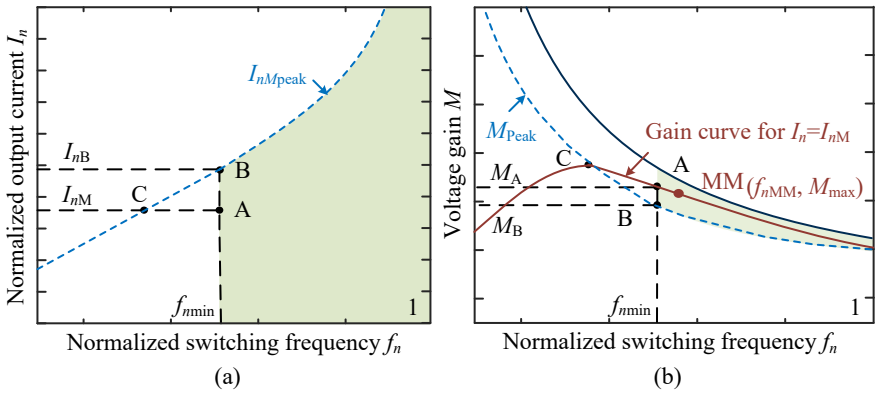

Figure 9. Distribution of working points in f_n-I_n and f_n-M for $I_{n\text{A}} \le I_{n\text{B}}$ (**a**) f_n-I_n. (**b**) f_n-M.

As shown in Figure 10, when $I_{n\mathrm{M}} > I_{n\mathrm{B}}$, the working condition at point C needs to be analyzed. In this case, if $M_{\mathrm{C}} \geq M_{\max}$ is satisfied, then $f_{n\mathrm{MM}} \geq f_{n\min}$, meaning that both switching frequency and voltage gain requirements are satisfied.

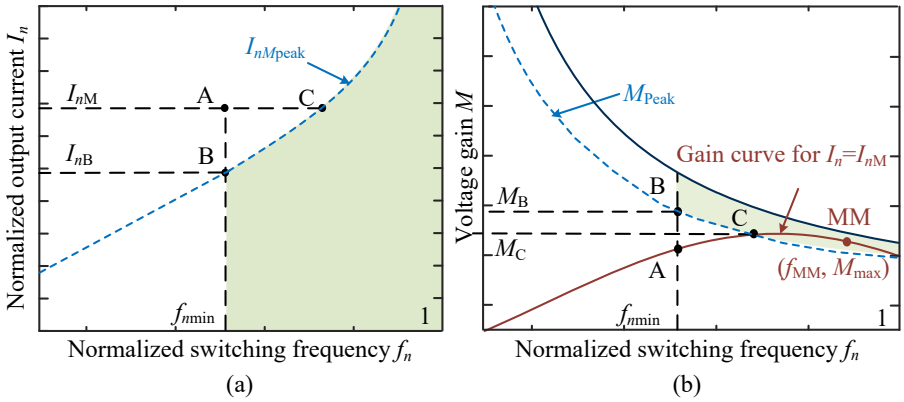

Figure 10. Distribution of working points in f_n-I_n and f_n-M for $I_{n\mathrm{A}} > I_{n\mathrm{B}}$ (**a**) f_n-I_n. (**b**) f_n-M.

According to the numerical calculation of the time domain model, different $M_{\mathrm{A}}/M_{\mathrm{C}}$ surfaces for k_m and Z_r can be obtained as shown in Figure 11. Taking the $M_{\mathrm{A}}/M_{\mathrm{C}}$ surface and the projection of the cross-section of $M_{\max}$ in the k_m-Z_r plane is the gain constraint curve in the BRR.

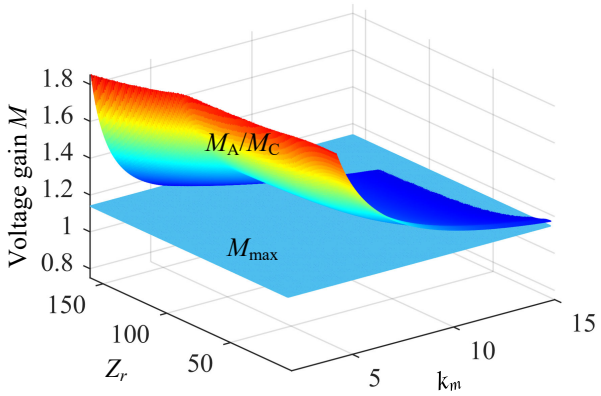

Figure 11. $M_{\mathrm{A}}/M_{\mathrm{C}}$ and $M_{\max}$ surfaces for voltage gain at different k_m and Z_r for n = 8.

In the ARR, the gain curve is monotonic, so only the requirement for the minimum voltage gain to be realized needs to be met, i.e., the voltage gain at light load at the maximum switching frequency is less than or equal to the required realized voltage gain. Here, the light load is set to 20% of the full load, i.e., $I_{n\mathrm{L}} = 0.2I_{n\mathrm{M}}$. The operating region above the light load is controlled by PFM, so only the minimum voltage gain that can be realized in the switching frequency range at light load needs to be considered.

Similar to the BRR, the critical operating conditions of the ARR can be categorized into two working conditions, L and Mm, as shown in Table 5. Here, L is the operating condition with the normalized output current $I_n = I_{n\mathrm{L}}$ at $f_{n\max}$, and Mm is the operating condition with voltage gain $M = M_{\min}$ at $I_n = I_{n\mathrm{L}}$.

Table 5. Key operating situations for forward mode in the BRR.

Operating Situations	Known Condition	Results of the Time-Domain Model Solution
L	$f_{n\max}$, $I_{n\mathrm{L}}$	M_{L}
Mm	$I_{n\mathrm{L}}$, $M_{\min}$	$f_{n\mathrm{Mm}}$

Figure 12 shows that if M_{L} is less than or equal to $M_{\min}$, the minimum voltage gain can be achieved from light load to full load within the given switching frequency range. The M_{L} and $M_{\min}$ surfaces at different k_m and Z_r can be obtained through numerical calculation, as shown in Figure 13. The constraint curve required to meet the minimum voltage gain requirement is obtained by projecting the curve obtained by intercepting the M_{L} surface in the k_m-Z_r plane at the $M_{\min}$ surface.

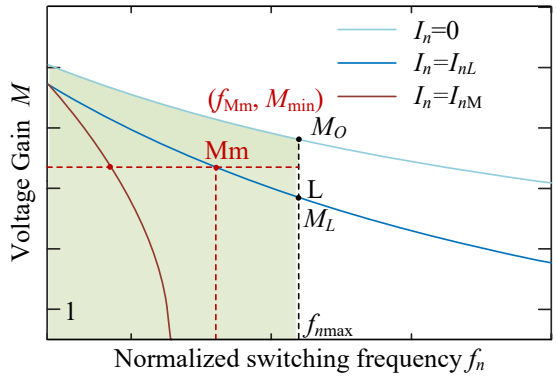

Figure 12. Voltage gain curves at light load and no load in the ARR.

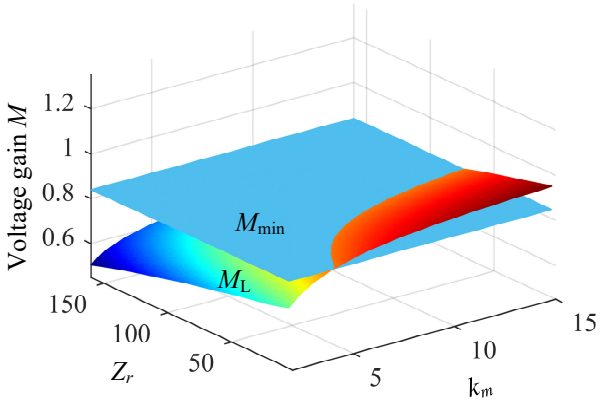

Figure 13. Surfaces corresponding to voltage gains M_{L} and $M_{\min}$ for different k_m and Z_r for $n = 8$.

Based on the above constraints, the preliminary parameter design space can be obtained for different turn ratios. The preliminary parameter constraint space is shown in Figure 14 for n = 8, for example.

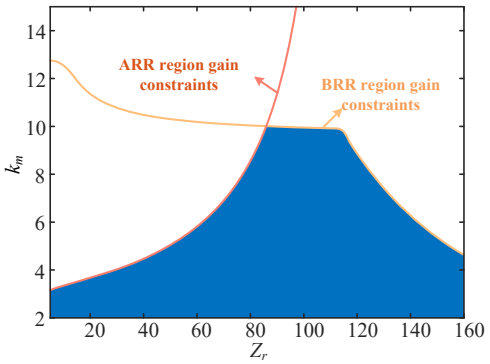

Figure 14. Z_r-k_m preliminary parameter constraint space when $n = 8$.

3.2.2. Searching for Optimization in Preliminary Parameter Design Space

Although the preliminary parameter design space has been able to satisfy the voltage gain condition, finding a set of parameters that lead to a better performance in the design space is still a necessity. Therefore, it is necessary to find the optimal set of solutions in the parameter design space based on the performance characterization of the device parameters, state variables, and so on. The device characteristics and key variables affected by the main circuit parameters are shown in Table 6 [9,19]. The variables $i_{Lr\mathrm{RMS}}$, $i_{Q1\mathrm{RMS}}$, $u_{Cr\max}$, and f_s mainly characterize the performance of the converter, which is dominated by the converter transfer efficiency under the determined circuit parameters.

Table 6. Key components and performance characterization parameters.

Components	Performance Characterization	Key Variables
L_r	winding losses and core losses	$i_{Lr\mathrm{RMS}}$, f_s
T	winding losses and core losses	$i_{Lr\mathrm{RMS}}$, $i_{Q_1\mathrm{RMS}}$, f_s
C_r	losses and maximum voltage stress	$i_{Lr\mathrm{RMS}}$, $u_{Cr\max}$
Primary side switches	conduction loss	$i_{Lr\mathrm{RMS}}$
Secondary side switches	conduction loss	$i_{Q_1\mathrm{RMS}}$

The selection of $i_{Lr\mathrm{RMS}}$, $i_{Q1\mathrm{RMS}}$, $u_{Cr\max}$, and f_s as the characterization indexes of performance allows the problem of determining the optimal solution in the preliminary parametric design space to be transformed into a multi-objective optimization problem. The maximum value of the resonant capacitor peak voltage $u_{Cr\max}$ occurs at the operating point at which the output power is at its maximum, the output voltage is at its maximum, and the input voltage is at its minimum, i.e., the operating point MM in Table 4. To facilitate the analysis, the resonant capacitor voltage stress requirement is transformed into a constraint. According to the input voltage level of 400 V, the resonant capacitor with a rated voltage of 1000 V is selected, and considering a certain margin, the resonant capacitor voltage constraint is selected as $u_{Cr\max} \leq 750$ V.

Considering the application scenario, this study focuses on optimizing working conditions in which the battery predominantly operates in constant power mode. It selects the working points at maximum and minimum voltage gain full load for optimization, denoted as points a and b. Consequently, parameter optimization is formulated as a multi-objective optimization function, as shown below:

$$\begin{aligned} &\min \mathrm{F}(x) = (f_1(x), f_2(x), f_3(x)) \\ &f_1(x) = {i_{Q_1\mathrm{RMSa}}}^2 + {i_{Q_1\mathrm{RMSb}}}^2 \\ &f_2(x) = {i_{Lr\mathrm{RMSa}}}^2 + {i_{Lr\mathrm{RMSb}}}^2 \\ &f_3(x) = f_{n\mathrm{MM}} - f_{n\mathrm{Mm}} \\ &x = (n, Z_r, k_m) \\ &s.t.x \in \{x \in \Omega | g(x) = u_{Cr\max} - 750 \leq 0\} \end{aligned} \tag{9}$$

In this equation, $\mathrm{F}(\mathbf{x})$ represents the vector-valued function, where each $f_i(\mathbf{x})$ is the objective function, and f_1, f_2, and f_3 are three different evaluation metrics for the decision variable $\mathbf{x}$. f_1 is the sum of the rms values of the secondary switches currents under the a-case and b-case scenarios, f_2 is the sum of the rms values of the resonant inductor currents under the a-case and b-case scenarios, and f_3 is the difference between the maximum operating switching frequency and the minimum operating switching frequency. All objective functions are equally weighted, ensuring no single function is prioritized during optimization.

Intelligent optimization algorithms have advantages in solving global optimal solutions for multi-objective multidimensional problems, while most intelligent optimization algorithms solve optimal solutions in a continuous feasible solution space. For LLC resonant converter parameter design, however, the challenge arises because the feasible solution

space is discrete, not continuous. In light of this, the ANSGA-III optimization algorithm, known for its efficacy in multi-objective optimization within discrete spaces, is adopted to address this issue. How ANSGA-III is implemented has been described in detail in [17]. The principle of ANSGA-III operates as follows: Initially, a population of size N is randomly generated. Subsequent genetic operations—selection, crossover, and mutation—then guide the evolution towards the first generation of offspring, optimizing towards the solution. This optimization process iterates, progressively refining solutions. Detailed pseudo-code for ANSGA-III implementation is provided in Algorithm 1.

Algorithm 1 ANSGA-III Algorithm

Initialize:
  Generate initial population P_0
  Generate reference point set R
  Set generation counter: $t = 0$
Main Loop:
while termination criteria not met **do**
  Generate offspring Q_t from P_t using genetic operations (selection, crossover, mutation)
  Combine parent and offspring populations: $R_t = P_t \cup Q_t$
  Perform non-dominated sorting on R_t to form fronts $F_1, F_2, \ldots$
  Select Next-Generation Population:
    Initialize next-generation population $P_{t+1} = \emptyset$ and current front index $l = 1$
  while $|P_{t+1}| + |F_l| \leq N$ **do** ▷ N is the population size
    Add individuals in front F_l to P_{t+1}
    $l = l + 1$
  end while
  if $|P_{t+1}| < N$ **then**
    Fill P_{t+1} with individuals from F_l based on reference-point association and niching until $|P_{t+1}| = N$
  end if
  $t = t + 1$
end while
Output:
Output non-dominated individuals in P_t as the Pareto optimal set

The Pareto surface, obtained through optimization with ANSGA-III, is depicted in Figure 15. Projections of this optimal set on the f_1-f_2 and f_2-f_3 planes are illustrated in Figures 16 and 17, respectively. Analysis reveals that at the point with the smallest sum of resonant inductor current RMS values (f_2), the sum of secondary switching current RMS values (f_1) is at its largest. Similarly, a smaller normalized switching frequency range correlates with a larger f_2 value. The three optimization objectives are in conflict; no single solution simultaneously minimizes them all. Thus, selecting an appropriate operating point requires a compromise based on specific demands.

Building a loss model based on the actual device mitigates subjective selection from the optimal solution set, though it increases the workload and may introduce inaccuracies. Thus, prioritizing generality, we chose optimized circuit parameters for the experimental platform through compromise. A point with a narrow switching-frequency range was selected to ensure low RMS current values, as indicated by the red dots in Figures 15–17, corresponding to the normalized circuit parameters [n, k_m, Z_r] = [8.5, 3.00, 123.9]. The chosen resonance frequency was 95 kHz, which resulted in the circuit parameters L_r, C_r, and L_m being 207.6 µH, 18.59 nF, and 622.7 µH. In addition, it was verified that the circuit parameters can satisfy the ZVS realization conditions with the selected switching model.

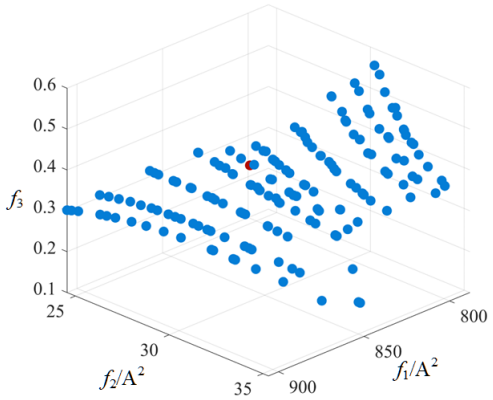

Figure 15. The Optimal set of objective functions obtained by ANSGA-III.

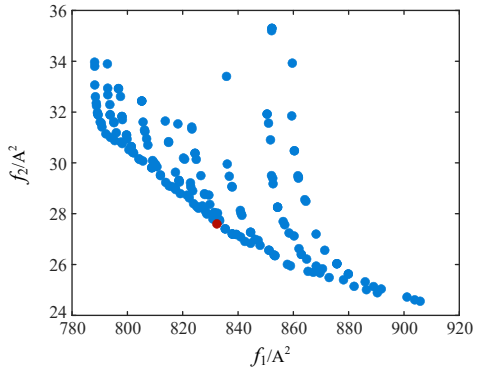

Figure 16. The optimal set of objective functions in the f_1-f_2 plane.

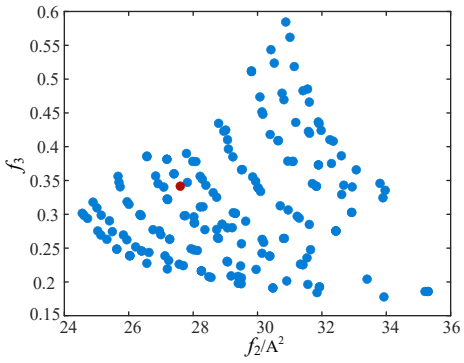

Figure 17. The optimal set of objective functions in the f_2-f_3 plane.

4. Experimental Results

To validate the proposed parametric design method, a 1200 W experimental prototype was developed, with its construction detailed in Figure 18. The primary control chip utilized was the TMS320F28335 from Texas Instruments, based in Dallas, TX, USA, complemented by Novosns's NSI1311 chip, Suzhou, China, for input and output DC voltage sampling, and ALLEGRO's ACS758 series chips from Manchester, United States, for AC current sampling, ensuring precise measurement and control. The sampling system and control chip facilitate precise output and synchronous rectification control of the converter. The experimental setup employed a Chroma 62050H from Taoyuan, Taiwan, China, as the DC input power supply, an ITECH brand programmable DC electronic load, and a YOKOGAWA DLM2024 oscilloscope from Tokyo, Japan for data acquisition. Table 7 details the final circuit parameters and semiconductor devices used. For testing, the DC power

supply (U_1) was set at 400 V, with the connected electronic load (U_2) variably programmed to range from 42 to 57 V across different load scenarios.

Table 7. Key components and performance characterization parameters.

Components	Parameter/Part#
Turns ratio n	8.5
Excitation inductor L_m	623.2 µH
Resonant inductor L_r	212.3 µH
Resonant capacitor C_r	212.3 nF
Resonant frequency f_r	94.76 kHz
Theoretical switching frequency f_s	78.35–110.05 kHz
Transformer cores	PQ5050 PC95
Inductive cores	PQ3535 PC95
Primary side switches	ROHM SCT3060AR
Secondary side switches	CRMICRO CRST045N10N

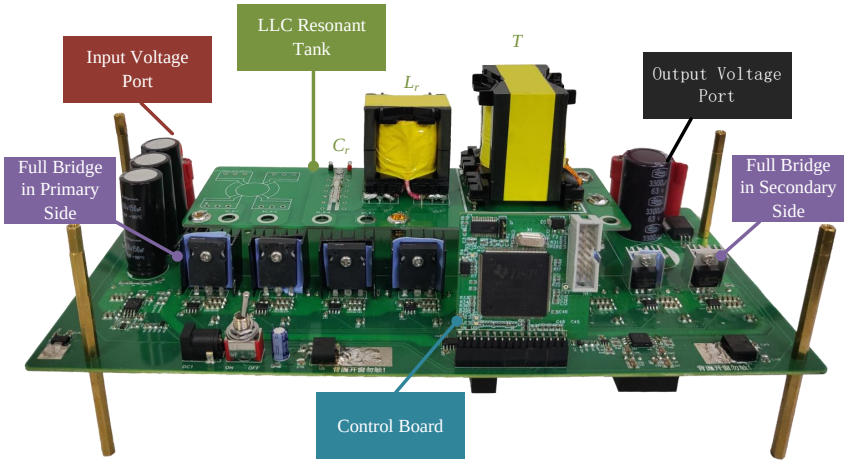

Figure 18. Experimental prototype of LLC resonant converter.

Figures 19–21 display the voltage and current measurement waveforms under 1200 W, 600 W, and 240 W load conditions, respectively. As demonstrated, both maximum and minimum gains, which are crucial for operational efficiency within the specified power range, successfully enable ZVS on the primary-side switches. Figures 19a, 20a and 21a illustrate that, at the moment the secondary-side switches turn off, the current i_2 reaches 0, achieving ZCS on the secondary side.

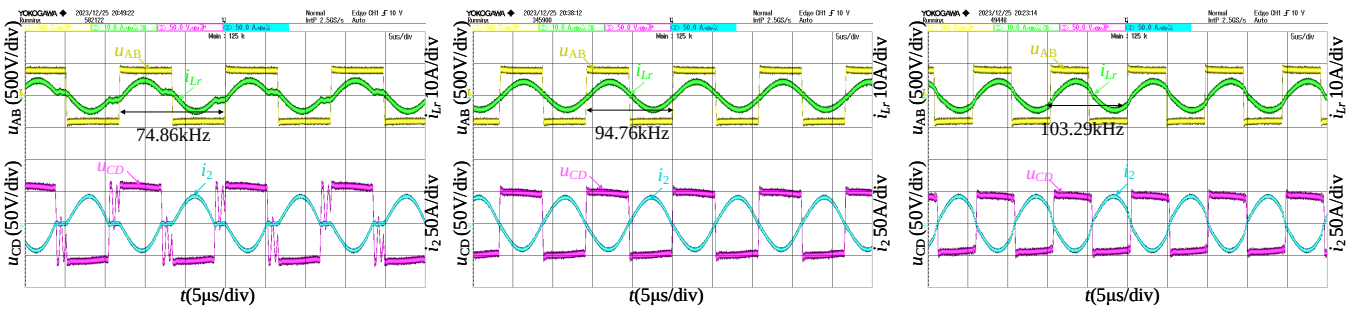

Figure 19. Key waveforms of the LLC prototype under 1200 W load condition in forward mode. (**a**) $U_1 = 400\,\text{V}$, $U_2 = 57\,\text{V}$, $M = 1.21125$. (**b**) $U_1 = 400\,\text{V}$, $U_2 = 47.06\,\text{V}$, $M = 1$. (**c**) $U_1 = 400\,\text{V}$, $U_2 = 42\,\text{V}$, $M = 0.8925$.

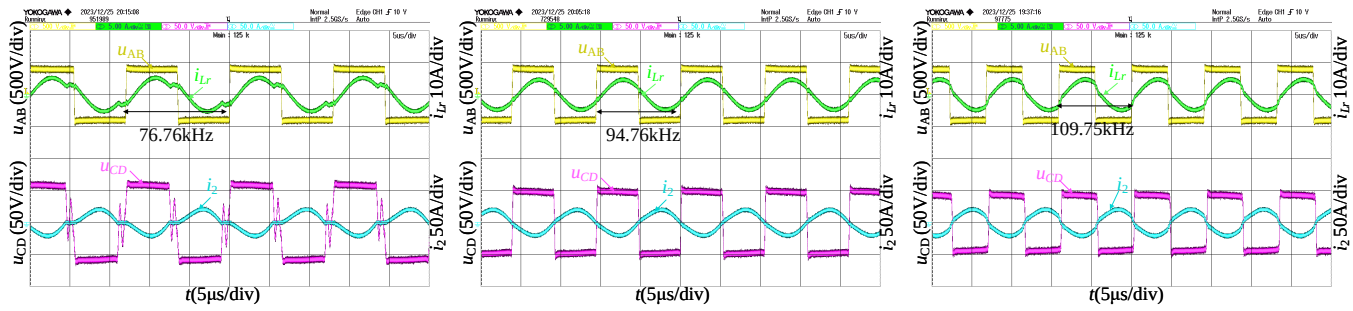

Figure 20. Key waveforms of the LLC prototype under 600 W load condition in forward mode. (**a**) $U_1 = 400\,\text{V}$, $U_2 = 57\,\text{V}$, $M = 1.21125$. (**b**) $U_1 = 400\,\text{V}$, $U_2 = 47.06\,\text{V}$, $M = 1$. (**c**) $U_1 = 400\,\text{V}$, $U_2 = 42\,\text{V}$, $M = 0.8925$.

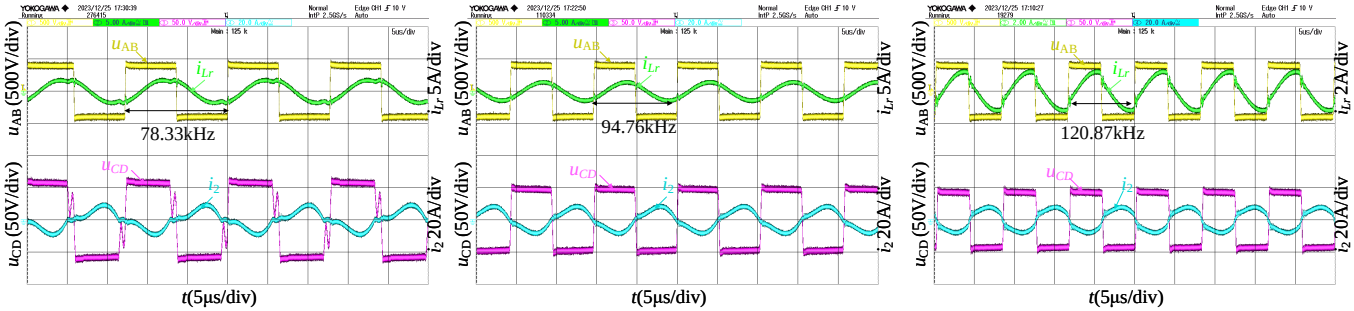

Figure 21. Key waveforms of the LLC prototype under 240 W load condition in forward mode. (**a**) $U_1 = 400\,\text{V}$, $U_2 = 57\,\text{V}$, $M = 1.21125$. (**b**) $U_1 = 400\,\text{V}$, $U_2 = 47.06\,\text{V}$, $M = 1$. (**c**) $U_1 = 400\,\text{V}$, $U_2 = 42\,\text{V}$, $M = 0.8925$.

At maximum power, the highest voltage gain aligns with a switching frequency of 74.86 kHz, while at lighter loads, the lowest voltage gain matches a peak switching frequency of 120.87 kHz. The observed operational frequency range of 74.86 kHz to 120.87 kHz exceeds the theoretical range of 78.35 kHz to 110.05 kHz, which is attributed to the upward shift caused by parasitic parameters. Despite this, the practical and theoretical trends align closely, keeping the discrepancy within acceptable bounds.

Under an input voltage of $U_1 = 400\,\text{V}$, measurements were taken for the peak and RMS values of the resonant inductor current i_{Lr}, the secondary-side rectifier current i_2, and the resonant capacitor voltage u_{Cr} across loads of 1200 W, 600 W, and 240 W. Figure 22 displays the operating waveforms at a 1200 W load. Figure 22 illustrates that the peak voltage of the resonant capacitor reaches 755 V at full load. This results in a mere 0.6% deviation from the theoretical design value of 750 V, affirming that the discrepancy lies within an acceptable margin and fulfills the design criteria.

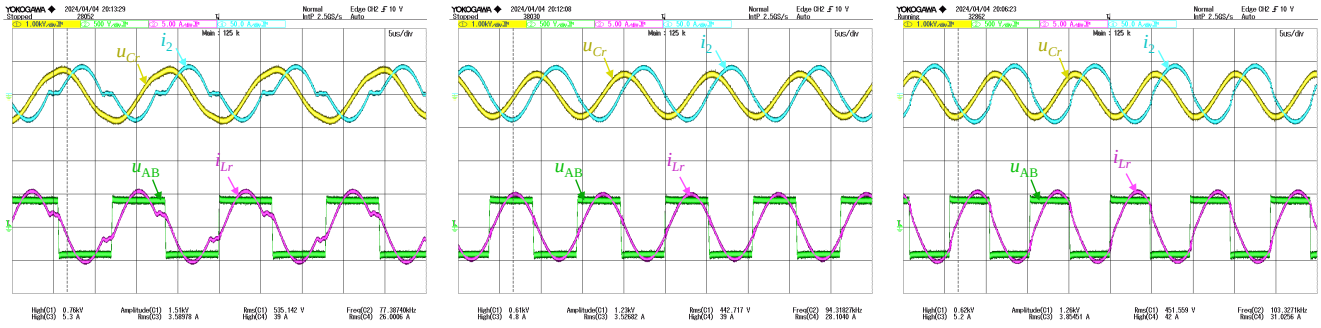

(a) (b) (c)

Figure 22. Key waveforms of the LLC prototype under 1200 W load condition in forward mode. (**a**) $U_2 = 57\,\text{V}$, $i_{Lr\text{RMS}} = 3.590\,\text{A}$, $i_{2\text{RMS}} = 26.000\,\text{A}$, $u_{Cr\text{peak}} = 755\,\text{V}$. (**b**) $U_2 = 47.06\,\text{V}$, $i_{Lr\text{RMS}} = 3.527\,\text{A}$, $i_{2\text{RMS}} = 28.104\,\text{A}$, $u_{Cr\text{peak}} = 610\,\text{V}$. (**c**) $U_2 = 42\,\text{V}$, $i_{Lr\text{RMS}} = 3.854\,\text{A}$, $i_{2\text{RMS}} = 31.026\,\text{A}$, $u_{Cr\text{peak}} = 620\,\text{V}$.

To assess the accuracy of the theoretical analysis, experimental data were compared with calculations from the time-domain analysis model. This comparison for the resonant inductor current RMS ($i_{Lr\text{RMS}}$), the secondary-side rectifier current RMS ($i_{2\text{RMS}}$), and the resonant capacitor peak voltage ($u_{Cr\text{peak}}$) is illustrated in Figures 23–25. At a 240 W load, the measured values fell below theoretical predictions due to reduced efficiency and heightened parasitic capacitance impact. However, the discrepancy between theoretical and actual measurements for $i_{Lr\text{RMS}}$, $i_{2\text{RMS}}$, and $u_{Cr\text{peak}}$ at 600 W and 1200 W loads was minimal, with errors of 0.88%, 1.12%, and 0.84%, respectively. These findings underscore the theoretical analysis and calculations' crucial role in guiding actual parameter design.

Figure 26 presents the operating efficiency curves for the LLC prototype across various load conditions and output voltages, employing a time-domain model for synchronous rectification control on the secondary side, with a maximum transfer efficiency of 96.54%. The overall efficiency remains high across most conditions, dipping only under light loads due to the predominance of iron losses, which fluctuate minimally with load variation. As the load escalates, rising conduction losses reduce the relative impact of iron losses, initially boosting efficiency. However, further load increases eventually lead to diminishing efficiency.

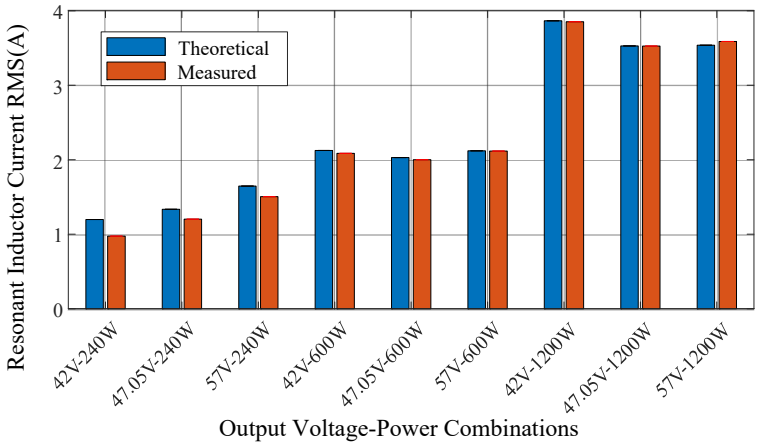

Figure 23. Comparison of measured and theoretical RMS values of resonant inductor currents for different combinations of output voltage and power.

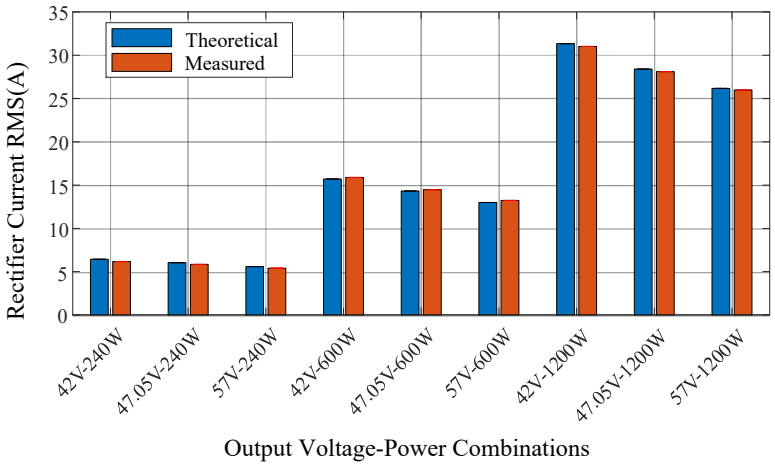

Figure 24. Comparison of measured and theoretical RMS values of rectifier currents on the verside side for different output voltage and power combinations.

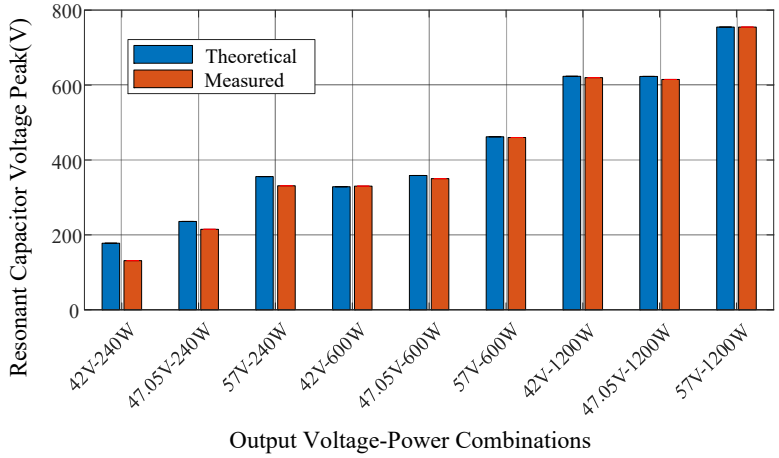

Figure 25. Comparison of measured and theoretical peak values of resonant capacitor voltage for different combinations of output voltage and power.

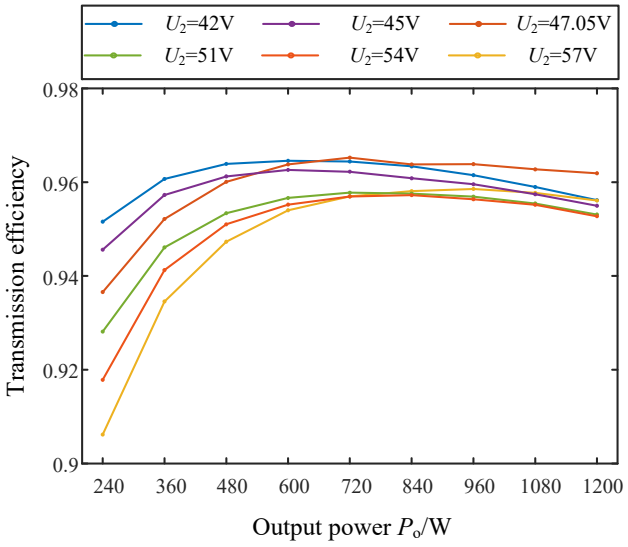

Figure 26. Efficiency curves.

5. Discussions

In practice, circuit parameters, including capacitance and inductance, often exhibit tolerances. Given the critical role of voltage gain in converter design, this analysis focuses on the impact of circuit parameter tolerances on voltage gain. It is assumed that minor variations in circuit parameters have a monotonic and independent impact on voltage gain. Figure 27, Figure 28 and Figure 29 illustrate the impact of tolerances in L_r, C_r, and L_m on the gain curves, respectively.

The analysis, focusing on the impact of tolerances in L_r, C_r, and L_m on voltage gain as depicted in Figures 27–29, reveals that within a 5% tolerance, the percentage errors within the voltage gain range do not exceed 1.07%, 0.16%, and 1.05%, respectively. Expanding the voltage gain range to 120% of its design specifications, to assess the design's resilience, results in only marginal error increases: 1.67% for L_r, 1.63% for L_m, and 0.46% for C_r.

Consequently, this detailed analysis confirms that the effects of circuit parameter tolerances on voltage gain are within manageable bounds, underscoring their adherence to the stringent specifications essential for optimal converter design.

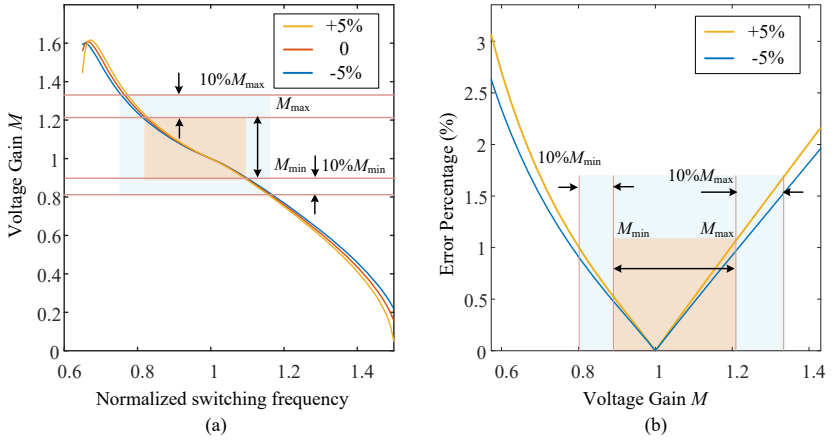

Figure 27. Effect of circuit parameter L_r tolerance on the gain curve. (**a**) Voltage gain curves at 5% tolerances. (**b**) Variation in voltage gain error percentage with voltage gain at 5% tolerance.

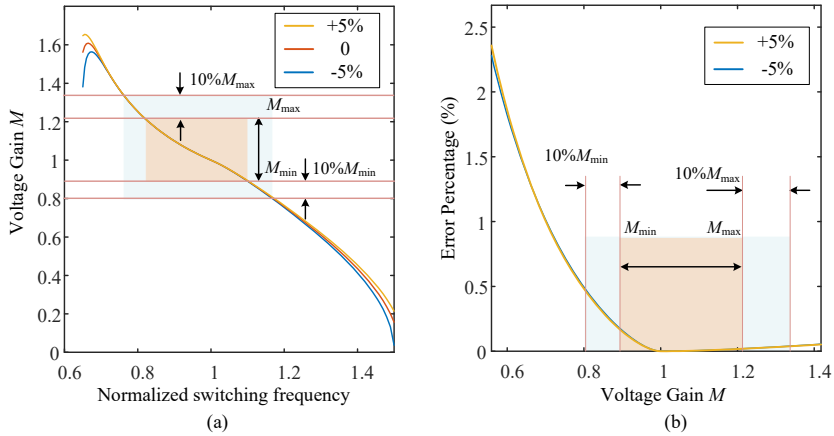

Figure 28. Effect of circuit parameter C_r tolerance on the gain curve. (**a**) Voltage gain curves at 5% tolerances. (**b**) Variation in voltage gain error percentage with voltage gain at 5% tolerance.

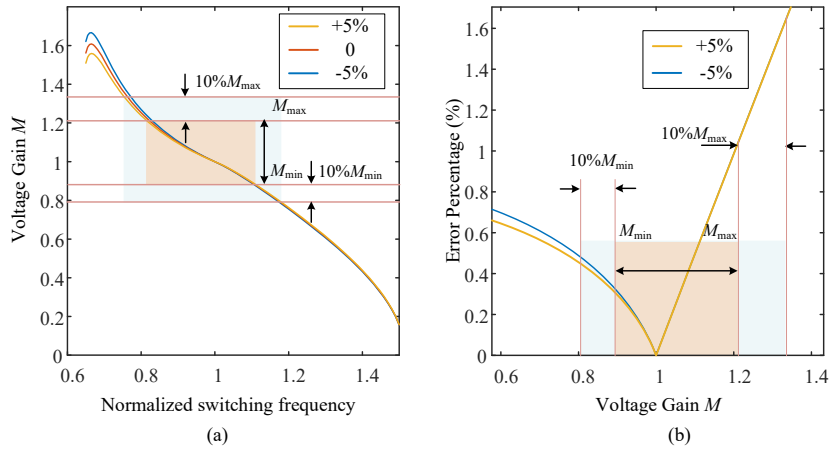

Figure 29. Effect of circuit parameter L_m tolerance on the gain curve. (**a**) Voltage gain curves at 5% tolerances. (**b**) Variation in voltage gain error percentage with voltage gain at 5% tolerance.

6. Conclusions

This paper proposes a multi-objective parameter optimization design method for the LLC resonant converter under PFM modulation, utilizing a step-by-step approach based on a time-domain model. First, a complete time-domain analysis model is established for the parameter design requirements. Second, based on the established time-domain model, the voltage gain is required to be the first layer of constraints, and the preliminary parameter design space that meets the most basic requirements is constrained. Then, taking the resonant inductor current and switching tube current, as well as the switching frequency range, as the optimization objectives, and taking the peak resonant capacitor voltage as the constraints, the intelligent optimization algorithm is used to find the optimum in the preliminary constrained parameter design space. Experimental validation confirms the method's effectiveness, achieving an impressive maximum efficiency of 96.54%. The design method proposed in this paper has the following advantages:

1. This method hierarchically optimizes design parameters, considering multiple factors including the switching frequency—unlike methods focusing solely on converter loss—thus enabling more versatile parameter selection without predetermining device choices;
2. Utilizing the ANSGA-III algorithm, the method outperforms exhaustive search techniques by efficiently identifying global optima within the discrete solution space, significantly reducing optimal search time.

However, there is room for improvement in the proposed methodology.

1. The current time-domain model overlooks the impact of parasitic capacitance and transmission loss, leading to theoretical switching frequencies under light loads that are lower than those observed in practice. Future iterations should account for these factors, allowing for a margin in practical applications.
2. Building on this method, converter efficiency could be further enhanced through the optimization of magnetic device design.

Author Contributions: Conceptualization, M.Y. and Q.L.; methodology, M.Y.; software, M.Y.; validation, M.Y.; data curation, M.Y.; writing—original draft preparation, M.Y.; writing—review and editing, Q.L.; project administration, Q.L. All authors have read and agreed to the published version of the manuscript.

Funding: This research was funded by Chongqing Municipal Technology Innovation and Application Development Special Key Project OF FUNDER grant number CSTB2023TIAD-KPX0083.

Data Availability Statement: The original contributions presented in the study are included in the article, further inquiries can be directed to the corresponding author.

Conflicts of Interest: The authors declare no conflicts of interest.

Appendix A

The equations of state for the P and N stages are shown below:

$$\begin{cases} \dot{i}_{Lr} = \dfrac{u_{La} - u_{Cr} - u_{Lm}}{L_r} \\ \dot{i}_{Lm} = \dfrac{u_{Lm}}{L_m} \\ \dot{u}_{Cr} = \dfrac{i_{Lr}}{C_r} \end{cases} \tag{A1}$$

Here $u_{Lm} = nu_2$ for P stage and $u_{Lm} = -nu_2$ for N stage, and the time-domain equations for P stage can be obtained after the normalization process as shown in

$$\begin{cases} i_{LrPn}(\theta) = P_1 \sin(\theta) + P_2 \cos(\theta) \\ u_{CrPn}(\theta) = -P_1 \cos(\theta) + P_2 \sin(\theta) + 1 - M \\ i_{LmPn}(\theta) = P_3 + M\theta/k_m \\ u_{LmPn}(\theta) = M \end{cases} \tag{A2}$$

where P_1, P_2, P_3, and P_4 are unknowns that need to be determined based on the stage operating conditions.

The time-domain equations for N stage are as follows.

$$\begin{cases} i_{LrNn}(\theta) = N_1 \sin(\theta) + N_2 \cos(\theta) \\ u_{CrNn}(\theta) = -N_1 \cos(\theta) + N_2 \sin(\theta) + 1 + M \\ i_{LmNn}(\theta) = N_3 - M\theta/k_m \\ u_{LmNn}(\theta) = -M \end{cases} \tag{A3}$$

Similarly, N_1, N_2, N_3, and N_4 are unknowns, and it can be found that the only difference between N stage and P stage is the sign of M, since u_2 is clamped to -U_2, rather than U_2, in the N stage.

As shown in Figure 2, different from the P or N stage, the output current of the O stage is cut off. The normalized special solution of the O stage is derived in

$$\begin{cases} i_{LrOn}(\theta) = i_{LmOn}(\theta) = O_1 \sin\left(\theta/\sqrt{k_m+1}\right) \\ \qquad + O_2 \cos\left(\theta/\sqrt{k_m+1}\right) \\ u_{CrOn}(\theta) = \sqrt{k_m+1}\left[O_2 \sin\left(\theta/\sqrt{k_m+1}\right)\right. \\ \qquad \left. -O_1 \cos\left(\theta/\sqrt{k_m+1}\right)\right] + 1 \\ u_{LmOn}(\theta) = \dfrac{k_m}{\sqrt{k_m+1}}\left[O_1 \cos\left(\theta/\sqrt{k_m+1}\right)\right. \\ \qquad \left. -O_2 \sin\left(\theta/\sqrt{k_m+1}\right)\right] \end{cases} \tag{A4}$$

where O_1 and O_2 are also unknowns.

Appendix B

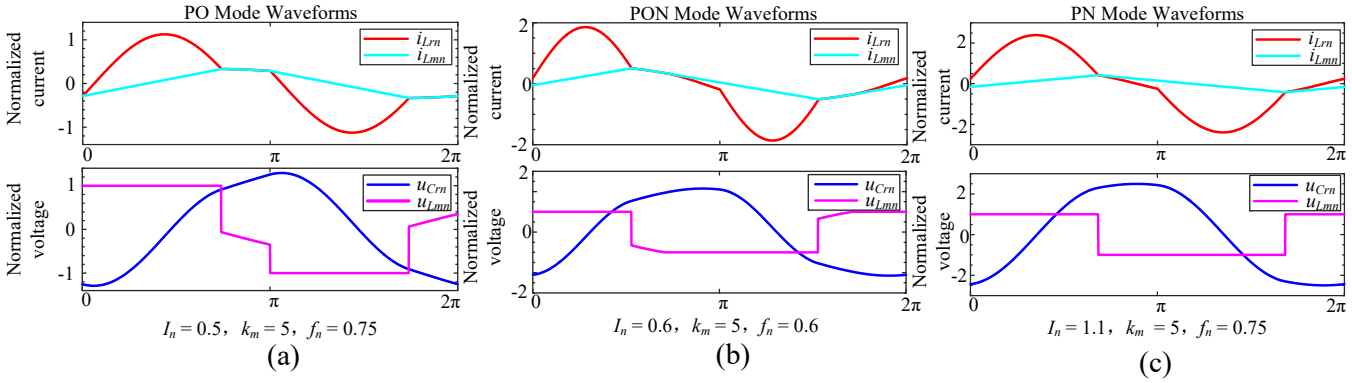

Figure A1. Normalized circuit waveforms for different modes under PFM modulation. (**a**) PO mode. (**b**) PON mode. (**c**) PN mode.

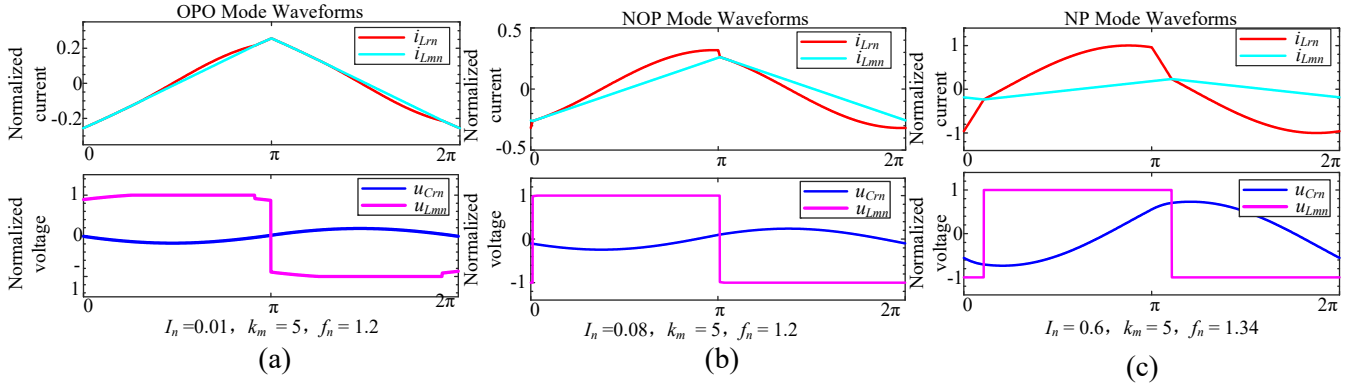

Figure A2. Normalized circuit waveforms for different modes under PFM modulation. (**a**) OPO mode. (**b**) NOP mode. (**c**) NP mode.

References

1. Wei, Y.; Luo, Q.; Wang, Z.; Mantooth, H.A. A Complete Step-by-Step Optimal Design for LLC Resonant Converter. *IEEE Trans. Power Electron.* **2021**, *36*, 3674–3691. [CrossRef]
2. Zhu, T.; Zhuo, F.; Zhao, F.; Wang, F.; Yi, H.; Zhao, T. Optimization of Extended Phase-Shift Control for Full-Bridge CLLC Resonant Converter with Improved Light-Load Efficiency. *IEEE Trans. Power Electron.* **2020**, *35*, 11129–11142. [CrossRef]
3. Lin, F.; Zhang, X.; Li, X.; Ma, H.; Cai, C. Design of Symmetrical CLLC-Resonant DC Transformer Considering Voltage Transfer Ratio and Cascaded System Stability. *IEEE Trans. Ind. Electron.* **2022**, *69*, 463–474. [CrossRef]
4. Jiang, T.; Zhang, J.; Wu, X.; Sheng, K.; Wang, Y. A Bidirectional LLC Resonant Converter with Automatic Forward and Backward Mode Transition. *IEEE Trans. Power Electron.* **2015**, *30*, 757–770. [CrossRef]
5. Zhu, T.; Zhuo, F.; Zhao, F.; Wang, F.; Yi, H. Analysis and Design of Multiple Phase-Shift Control for CLLC Resonant Converter Under Light-Load Conditions Based on Multi-Harmonic Impedance Model. *Proc. CSEE* **2021**, *41*, 326–339. [CrossRef]
6. Fang, X.; Hu, H.; Shen, Z.J.; Batarseh, I. Operation Mode Analysis and Peak Gain Approximation of the LLC Resonant Converter. *IEEE Trans. Power Electron.* **2012**, *27*, 1985–1995. [CrossRef]
7. Fang, X.; Hu, H.; Shen, J.; Batarseh, I. An Optimal Design of the LLC Resonant Converter Based on Peak Gain Estimation. In Proceedings of the 2012 Twenty-Seventh Annual IEEE Applied Power Electronics Conference and Exposition (APEC), Orlando, FL, USA, 5–9 February 2012; pp. 1286–1291. [CrossRef]
8. Fang, X.; Hu, H.; Chen, F.; Somani, U.; Auadisian, E.; Shen, J.; Batarseh, I. Efficiency-Oriented Optimal Design of the LLC Resonant Converter Based on Peak Gain Placement. *IEEE Trans. Power Electron.* **2013**, *28*, 2285–2296. [CrossRef]
9. Yu, R.; Ho, G.K.Y.; Pong, B.M.H.; Ling, B.W.K.; Lam, J. Computer-Aided Design and Optimization of High-Efficiency LLC Series Resonant Converter. *IEEE Trans. Power Electron.* **2012**, *27*, 3243–3256. [CrossRef]
10. Deng, J.; Li, S.; Hu, S.; Mi, C.C.; Ma, R. Design Methodology of LLC Resonant Converters for Electric Vehicle Battery Chargers. *IEEE Trans. Veh. Technol.* **2014**, *63*, 1581–1592. [CrossRef]
11. Fang, Z.; Tao, C.; Duan, S.; Chen, C. Optimal Design Methodology for LLC Resonant Converter in Battery Charging Applications Based on Time-Weighted Average Efficiency. *IEEE Trans. Power Electron.* **2015**, *30*, 5469–5483. [CrossRef]

12. Hu, Z.; Wang, L.; Qiu, Y.; Liu, Y.F.; Sen, P.C. An Accurate Design Algorithm for LLC Resonant Converters—Part II. *IEEE Trans. Power Electron.* **2016**, *31*, 5448–5460. [CrossRef]
13. Menke, M.F.; Duranti, J.P.; Roggia, L.; Bisogno, F.E.; Tambara, R.V.; Seidel, A.R. Analysis and Design of the LLC LED Driver Based on State-Space Representation Direct Time-Domain Solution. *IEEE Trans. Power Electron.* **2020**, *35*, 12686–12701. [CrossRef]
14. Zhou, B.; Zhang, M.; Luo, H.; Qiu, Y.; Chen, S.; Zang, T.; Zhou, Y.; Zhou, X. Multi-objectives Optimization of Parameter Design for LLC Converter Based on Data-driven Surrogate Model. *IET Power Electron.* **2023**, pel2.12525. [CrossRef]
15. Wei, Y.; Pereira, T.; Pan, Y.; Liserre, M.; Blaabjerg, F.; Mantooth, H.A. A General and Automatic RMS Current Oriented Optimal Design Tool for LLC Resonant Converters. *IEEE J. Emerg. Sel. Top. Power Electron.* **2022**, *10*, 7318–7332. [CrossRef]
16. Jiao, J.; Guo, X.; Wang, C.; You, X. Time-Domain Analysis and Optimal Design of LLC-DC Transformers (LLC-DCXs) Considering Discontinuous Conduction Modes. *IEEE Trans. Transp. Electrif.* **2023**, *9*, 2308–2323. [CrossRef]
17. Cheng, Q.; Du, B.; Zhang, L.; Liu, R. ANSGA-III: A Multiobjective Endmember Extraction Algorithm for Hyperspectral Images. *IEEE J. Sel. Top. Appl. Earth Obs. Remote Sens.* **2019**, *12*, 700–721. [CrossRef]
18. Tian, Y.; Zhu, W.; Zhang, X.; Jin, Y. A Practical Tutorial on Solving Optimization Problems via PlatEMO. *Neurocomputing* **2023**, *518*, 190–205. [CrossRef]
19. Yue, S.; Li, Y.; Yang, Q.; Yu, X.; Zhang, C. Comparative Analysis of Core Loss Calculation Methods for Magnetic Materials Under Nonsinusoidal Excitations. *IEEE Trans. Magn.* **2018**, *54*, 6300605. [CrossRef]